energies

MDPI

Article

Prototype of a Two-Phase Axial-Gap Transverse Flux Generator Based on Reused Components and 3D Printing

Víctor Ballestín-Bernad, Jesús Sergio Artal-Sevil and José Antonio Domínguez-Navarro *

Department of Electrical Engineering, School of Engineering and Architecture, University of Zaragoza, C/María de Luna, 50018 Zaragoza, Spain
* Correspondence: jadona@unizar.es

Abstract: This paper presents a prototype of a low-cost two-phase axial-gap transverse flux generator, in which the magnetic and electric circuits have been made of reused materials, and the stator housing has been manufactured by 3D printing of plastic. Therefore, this work presents as a novelty the combination of the novel transverse flux topology and two challenging trends in electrical machines manufacturing, such as reusing of components and additive manufacturing. Axial-gap transverse flux machines potentially enable the combination of two of the main advantages of axial flux machines and transverse flux machines, i.e., short axial length and a high number of poles. The two-phase arrangement with shared air gap is of great interest in order to reduce further the axial length while avoiding the use of magnetic materials in the rotor, such as iron or soft magnetic composites. However, the equivalent air gap might be large, with significant leakage and fringing effects as the magnetic flux closes through the air. Therefore, in this paper the accuracy of the analytical equations and the magnetic equivalent circuit is firstly investigated. The two-phase axial-gap transverse flux machine is prone to misalignment between phases and rotor imbalances that alter the air gap length, so these effects have been included in the simulations with the finite element method. Experimental tests have been conducted throughout the investigation, from the prototype characterization to the steady-state operation, both with no load and with resistive loads.

Keywords: transverse flux machines; prototype; 3D printing; additive manufacturing; electric generator; finite element method

Citation: Ballestín-Bernad, V.; Artal-Sevil, J.S.; Domínguez-Navarro, J.A. Prototype of a Two-Phase Axial-Gap Transverse Flux Generator Based on Reused Components and 3D Printing. *Energies* **2023**, *16*, 1594. https://doi.org/10.3390/en16041594

Academic Editors: Christopher H.T. Lee, Yuting Gao, Dawei Li and Libing Jing

Received: 12 January 2023
Revised: 31 January 2023
Accepted: 3 February 2023
Published: 5 February 2023

1. Introduction

Transverse flux machines (TFMs) have been proposed in the electric machinery literature for many low-speed, high-torque applications, from electric vehicle powertrains to wind power generation [1,2], with particular interest in direct-drive systems [3]. TFMs enable the allocation of a high number of poles, due to the decoupling of the magnetic and electrical loadings, thus resulting in a high torque density. However, TFMs are still challenging in terms of manufacturing (tolerances and materials) and control (high torque ripple and low power factor).

Most of the electric machinery design methodologies are based on some basic steps: definition of the machine specifications, selection of the topology, analytical and/or finite element (FE) modeling, optimization, and finally prototyping and experimental tests. The prototype construction and testing are key stages, as they serve in most cases to validate the design methodology or to go further in the analysis.

In the field of TFMs, some remarkable TFM prototypes can be found in the recent literature. In [4], a TFM with a claw-pole stator is proposed and experimentally validated as a motor for robotic applications. Several inner- and outer-rotor TFM prototypes are deeply analyzed and tested in [5–7]. The authors of [8] propose a two-phase TFM with skewed permanent magnets (PMs) and shared-border pole stator, showing a 2.6% error between the FE and the experimental effective value of the back electromotive force (back-EMF).

A TFM with a single-row of magnets (i.e., with half the magnets of conventional TFMs) is proposed in [9]. Under no load, the magnetic equivalent circuit and tests show a 9% discrepancy in the back-EMF, but FE analysis and tests show a perfect agreement. Under load, the FE versus experimental error becomes higher, and the same conclusion is drawn in [10].

In [11] two double-stator, flux-concentrating TFM prototypes with E- and quasi-U-shaped cores and variable air gap are tested after FE-based optimization—for cogging torque minimization—using the Taguchi method. A similar approach is used in [12] regarding Halbach arrays and stator elements optimization, and the topology is further investigated in [13] to reduce the cost and improve its thermal behavior. In [14] a passive rotor, flux-concentrating TFM is optimized with more design variables and objective functions, thus several well-known approximation models are used in order to reduce the computation cost. In this case, the errors in the generated power lie between 13 and 20% when comparing FE analysis and experiments.

According to the literature, there are some manufacturing defects that can affect significantly the performance of TFM prototypes. For example, in [15] the air gap between radial and axial cores and the angle error between rotor teeth and PMs result in a back-EMF peak value deviation around 9% from FE simulations. Moreover, the non-uniformity of the air gap causes an asymmetry between the fundamental waves of the back-EMF in the three phases, and the misalignment of the rotor elements is associated with angular shifts between phases other than ideal (120 electric degrees for three-phase machines) [16]. In [17], the PMs weakening and the increase in the armature winding due to heat are also pointed out as potential sources of error.

In multiphase stacking arrangements, the axial gap between phases can also affect the back-EMF amplitude [18]. The authors of [19] present a four-single-phase TFM with combined teeth, i.e., with no axial gap between each single-phase module. This topology is a flux-concentrating TFM with soft magnetic composite (SMC) cores, and its manufacturing and materials uncertainties are deeply studied in [20]. On the rotor side, the contact between PMs and the SMC cores might not be perfect, with small air gaps; the grinding of the SMC components might create a conducting skin; and the rotor body, made of titanium, could behave as an electrical conductor even though ideally it is not in the magnetic circuit. On the other hand, de-burring of the stator SMC cores might create more conducting skins, and segmentation of the stator cores might cause an elliptical outer geometry and small gaps between the stator segments. Furthermore, the iron losses on the machine SMC cores might differ from samples used to determine iron losses coefficients. There is a 23.7% errorbetween the FE and experimental back-EMF due to these manufacturing and material uncertainties. The authors of [21,22] describe similar problems (parasitic air gaps, oxidation layer in the SMC poles, and non-uniform air gap), and their experimental and simulation results show good agreement (the assembly effects are included in the simulation results).

Mechanical stability is also a critical aspect when manufacturing electric machines with disk-shaped rotors, as the high value of their diameter-to-length ratio make them to be strongly exposed by the inclined rotor fault [23]. In [24] the vibration and noise response of the TFMs proposed in [11,25] is measured with the help of an accelerometer and a microphone. Static and dynamic eccentricities of the TFM proposed in [9] are further studied in [23], and the severity of a dynamic eccentricity is evaluated experimentally.

Additive manufacturing (AM) has been recently introduced in the field of electrical machines in order to overcome the limitations of traditional manufacturing techniques and their effects on electric drives design and performance. In [26], a discussion about the technical and process challenges using conventional techniques in electrical machines manufacturing is presented, and several solutions are proposed based on additive manufacturing opportunities. Three main lines of research for AM in electrical machines are profusely described in [27,28], namely: mechanical assembly and thermal management, magnetic materials and winding, and insulation materials. The technology maturity is low at the moment, especially for the active parts (coils, cores, and PMs) when compared

with the passive parts (thermal and mechanical); however, AM enables further development of asymmetrical and special purpose machines against conventional induction and synchronous machines [29]. Despite the high potential of TFMs as special purpose machines with high torque density, few attempts have been made to introduce AM in TFMs construction. Three dimensional printing of plastic has been proven as a flexible and effective technique for the stator and/or rotor housings construction in some low-cost TFM prototypes [30–32].

Moreover, the industrial demand of electric motors and generators is constantly increasing, due to the worldwide expansion of new technologies such as electric vehicles and renewable power plants. In this context, the circular economy is currently a major concern for citizens and governments in order to reduce pressure on natural resources. For example, the European Commission identifies electrical equipment and vehicles as "key product value chains" in their Circular Economy Action Plan [33].

The electric machinery design models are mainly focused on high performance and compliance with specifications, and they rarely include design criteria related to sustainability. In [34], some ideas for subsequent recycling of the machines are given, such as the use of SMC cores, SmCo magnets, and stator segmentation. Specifically, a claw-pole TFM is proposed as a favorable topology to include these design issues, and it is compared with a reference machine. Moreover, some electric machines—or at least some of their components—can be directly reused in a different application: for example, after the end-of-life-cycle of an internal combustion engine, the rotor of a claw-pole alternator can be introduced in a conventional stator to build a small PM synchronous generator for wind energy harvesting [35].

The aim of this work is to present the feasibility of reused components and additive manufacturing in a novel TFM topology, such as the two-phase axial-gap transverse flux machine. The TFM prototype is fully characterized through experiments in order to validate the TFM construction and performance, and the accuracy of the analytical equations, the magnetic equivalent circuit and the finite element method is also investigated.

This paper is structured as follows. In Section 2, the design process of the low-cost two-phase axial-gap transverse flux generator (TPAGTFG) is described. In Section 3 the steady-state operation of the prototype is validated using analytical equations, the magnetic equivalent circuit, the finite element method, and experimental tests. Finally, in Section 4 the conclusions of this work are presented.

2. Design of a Low-Cost Transverse Flux Generator Prototype

The TPAGTFG proposed in this paper is designed to be built exclusively with reused materials, except the 3D-printed stator housings, so this is the only component of the prototype cost. The introduction of reused components aims to reduce significantly the cost—and the amount—of raw materials that are needed, and this can be of particular importance in TFMs, where cost and materials optimization plays a major role to compete with conventional induction and synchronous machines. More specifically, the basic U and I cores that characterize TFMs can be obtained from transformers, as both machines account for similar magnetic circuits. The application of reused components imposes some dimensions, therefore adding some constraints to the machine sizing, but it might be the price to pay for aligning electrical machines design with sustainability and circular economy goals. Moreover, the constraints imposed by the introduction of some reused components can be compensated by the flexibility of new additive manufacturing techniques that open the way to new geometries and materials.

In this work, the stator iron cores proceed from six small transformers previously used in old-fashioned halogen spotlights (Figure 1a) that have been recently replaced by LED technology. The windings and the central iron column have been removed with cutting tools from the initial iron blocks, then the U and I cores needed for the TFM construction are obtained (Figure 1b). The welds between the U and I cores have also been eliminated by cutting. Moreover, the stator copper, the PMs, the rotor housing (made of methacrylate),

and the mechanical support (axis, bearings, pulleys, and belt) come from different academic end-of-degree projects and master's theses, and the drive motor is a starter DC motor from an old car. Finally, the stator housing is manufactured by 3D printing using polylactic acid (PLA), a widely used filament material in the field of 3D printing that is recyclable and biodegradable. Figure 2 shows an overview of the TPAGTFG prototype.

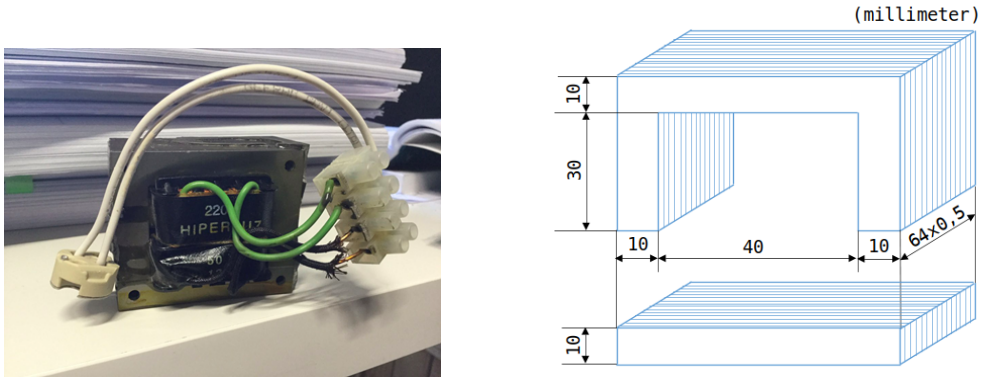

(**a**) (**b**)

Figure 1. (**a**) Reused transformer from a halogen spotlight. (**b**) Main dimensions of the transformer cores, with removed winding and central iron column.

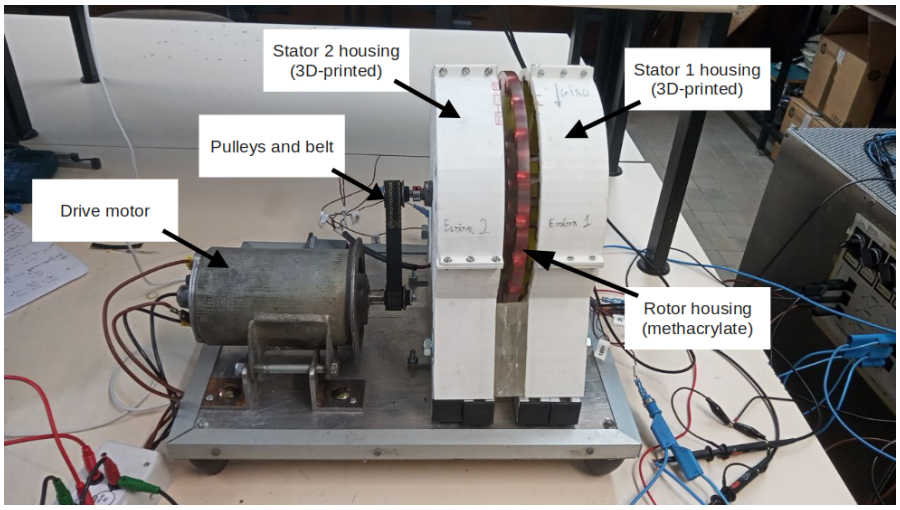

Figure 2. An overview of the TPAGTFG prototype.

2.1. Discussion on Transverse Flux Topologies

Figure 3a depicts one pole pair of a basic TFM in its linear version. The U-shaped stator core guides the magnetic flux from one PM to another, embracing the coil. Moreover, TFMs sometimes include some magnetic shunts, also named I cores or bridges (Figure 3b), that reduce the "negative flux" of the inactive magnets (those magnets that are not below the U cores in a given time). From this basic structure, a plethora of multi-pole and multi-phase TFM arrangements can be defined.

Figure 4 shows the most common transverse flux topologies for one pole pair and one phase stack, regarding the stator, rotor, and air gap arrangements. Double-sided stators require complex supports, and the assembly of many small pieces may become intricate, so these topologies are initially dismissed for the low-cost prototype of this work. Among the single-sided arrangements, the flux-concentrating options and the surface-mounted, radial gap options are also dismissed because they need a magnetic path through the rotor, thus iron or SMC pieces are required, increasing the number of small pieces and so the complexity of the assembly process. Therefore, single-sided, surface-mounted, and axial-gap TFMs are selected for further research. As there is no iron or SMC path through

the rotor, synthetic materials such as glass or plastic can be used exclusively for the rotor manufacturing, at the cost of a higher equivalent air gap (air plus magnets). However, such rotors may be lighter than the conventional ones.

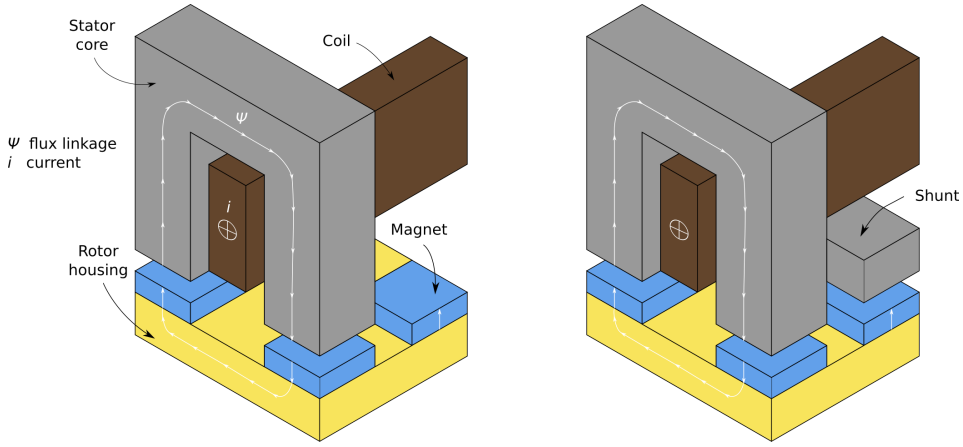

Figure 3. Basic TFM structure of one pole pair: (**a**) with no magnetic shunt and (**b**) with magnetic shunt.

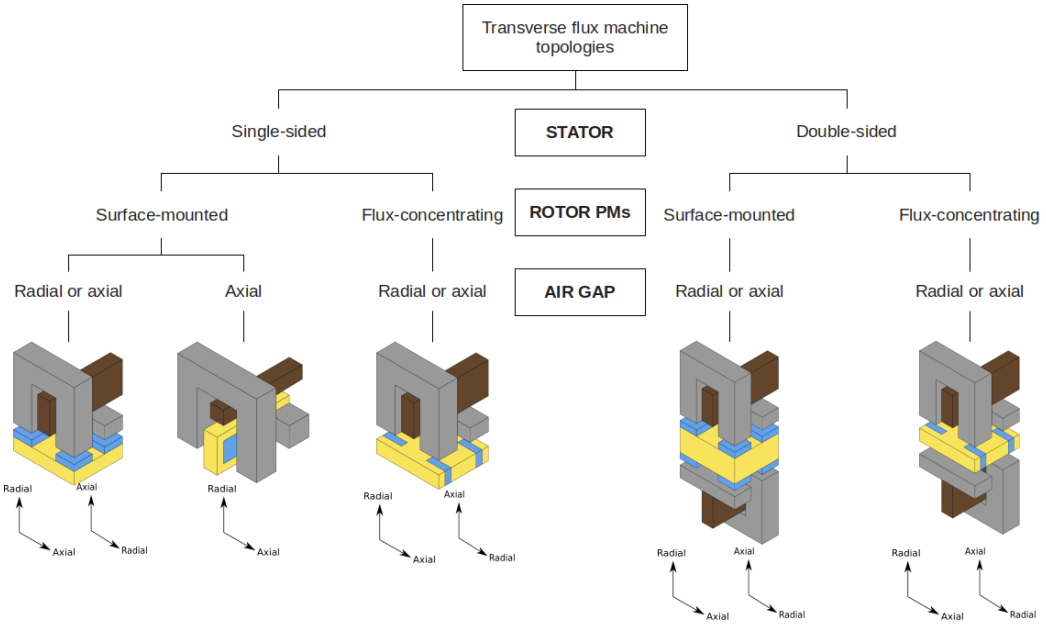

Figure 4. TFM topologies for one pole pair and one phase.

In this work, the starting point for the generator design are six transformers from halogen spotlights, as previously shown in Figure 1a. Each transformer core is made up of 64 iron sheets of 0.5 mm thickness, as shown in Figure 1b. Table 1 shows different combinations of the number of phases (m) and pole pairs (p), based on the available materials. According to (1), the number of U cores (u) is related to the number of "cuts" per transformer (c), i.e., the number of iron sheet "bundles" that are taken from each transformer core. Each iron sheet bundle has an axial length (L_u) given by (2). Moreover, there are different combinations of the number of phases and pole pairs, according to (3). All the proposed options in Table 1 have the same iron mass and torque, as the rated torque (T) of a TFM is approximately proportional to L_u, m, and p (4). N is the number of turns per phase, $B_{g,avg}$ is the average flux density in the air gap, H_{ul} is 10 mm as shown in Figure 1b, and I_q is the stator current in the quadrature-axis.

$$u = 6c \tag{1}$$

$$L_u = 0.5\text{ceil}(64/c) \tag{2}$$

$$p = u/m \tag{3}$$

$$T \approx \frac{m}{2} p(NpB_{g,avg}L_u H_{ul}) I_q \tag{4}$$

Single-phase topologies have been widely studied in the TFMs literature since the end of the 20th century, when TFMs started to gain more attention among researchers. Moreover, single-phase TFMs have no starting torque in motoring mode, as they usually work as synchronous machines. For these reasons, in this work single-phase TFMs have been dismissed. Moreover, most of the conventional three-phase TFMs in the literature show a stacking arrangement, i.e., three equal single-phase blocks that are axially stacked and circumferentially shifted in order to form an accurate multi-phase arrangement. This leads to TFMs with a high axial length, and this might not be adequate for some applications with space limitations, so other configurations should be investigated to address this problem. Consequently, among the two-phase topologies, the shared-gap arrangement (see Figure 5a) is preferred against the non-shared gap arrangement (Figure 5b), because the same air gap serves for both A and B phases, so the axial length of the machine might be reduced. Moreover, the PMs and the coil do not compete for the same space in a given slot size, potentially enabling higher electric and magnetic loadings.

Table 1. Available options for the TF generator design.

c	u	L_u (mm)	m	p
2	12	16	1 2 3	12 6 4
3	18	11	1 2 3	18 9 6
4	24	8	1 2 3	24 12 8

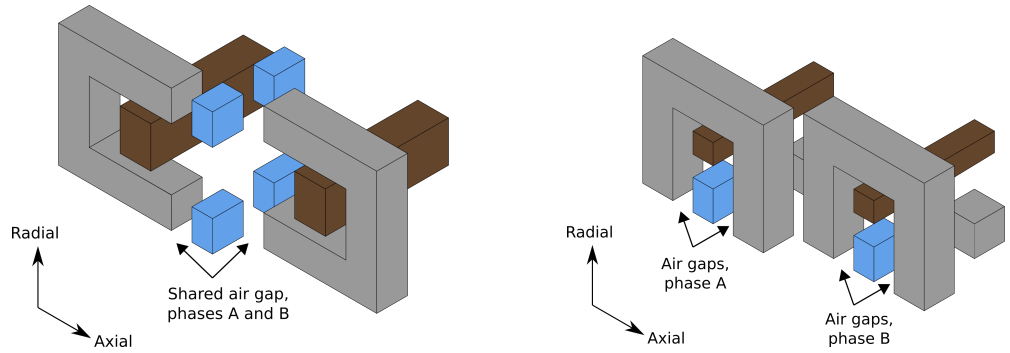

(**a**) (**b**)

Figure 5. (**a**) Shared-gap and (**b**) non-shared-gap arrangements for two-phase, axial-gap TFMs.

2.2. Proposed TPAGTFG

The two-phase, axial-gap TFM combines some features of the axial flux machines (short axial length) and the transverse flux machines (high number of poles), while keeping a non-zero starting torque due to the 90-degree shift between phases. This topology has been previously described in [36], but only a computational study was performed. Table 2

shows the main dimensions and ratings of the proposed TPAGTFG prototype. The rated speed is 500 rpm, so nine pole pairs have been selected, from among the previous options shown in Table 1, leading to a fundamental frequency below 100 Hz. At higher frequencies the iron losses and the eddy current losses in the PMs could become important [37]. The air gap length has been set to 10 mm in order to avoid excessive cogging torque and vibrations that could affect the plastic-made stator housing stability and the rotor eccentricity. This low-cost prototype with reused materials serves only as a first approximation to the topology, so the air gap length could be reduced in more advanced TPAGTFG models with more robust materials and precise manufacturing tools in order to increase the machine ratings. Moreover, the characterization of the PMs is of great importance, since the flux linkage produced by the PMs significantly affects the machine performance, even under no load. The remanent flux density of the PMs shown in Table 2 has been measured with the help of a gaussmeter, resulting in 0.6 T. It is a quite low value for NdFeB magnets, and it can be attributed to uncertainties, defects, or poor quality during manufacturing.

Table 2. Main TPAGTFG dimensions and ratings.

Number of phases	2	Air gap length	10 mm
Rated speed	500 rpm	PMs remanent flux density	0.6 T
Number of pole pairs	9	PMs axial length	12.5 mm
Fundamental frequency	75 Hz	PMs diameter	10 mm
Outer diameter	250 mm	Number of turns per phase	144
Axial length	150 mm	Wire diameter	1.45 mm (AWG15)

The CAD model of the proposed TPAGTFM is shown in Figure 6. The iron cores of phases A and B are shifted 90 electrical degrees in order to obtain an accurate two-phase arrangement. To minimize the rotor eccentricity, two disks made of methacrylate have been screwed to the rotor housing (see Figure 6a). Moreover, the stator housings have been divided into four parts due to limited space in the 3D printer plate, so they must be joined with screws through the ribs, as shown in Figure 6b. Due to 3D printing facilities, it is possible to leave some holes in the stator housing to improve the air circulation from the stator coils to the outside.

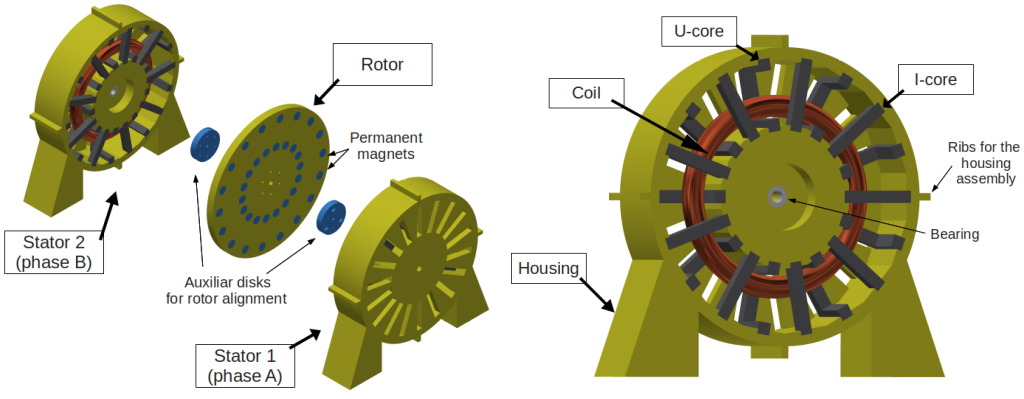

(**a**) (**b**)

Figure 6. CAD model of the proposed machine: (**a**) exploded view and (**b**) stator detail.

2.3. Prototyping and Characterization

Table 3 shows the main parameters of the 3D printer setup for the prototype construction. These were based on typical values for PLA and previous experience. It should

be noted that the mechanical stability of the stator is determined by the printer infill, the material properties, and the machining precision. Figure 7 shows the TPAGTFG prototype in more detail. After the assembly and subsequent adjustments, three manufacturing defects have been detected in the prototype: the electric angle between the phases is higher than 90 electrical degrees (misalignment), the air gap length is slightly higher in one of the phases (run-out fault), and the rotor is not strictly perpendicular to the rotation axis (inclined rotor fault). These kind of defects have been previously found in other TFM prototypes, as stated in Section 1. More specifically, according to the measurements using a caliper, the angular misalignment is 4.5 mechanical degrees, the air gap lengths are 9 and 11 mm (eccentricity factor 10%), and the rotor angle with respect to the axis is 89 degrees. The misalignment and the run-out fault have been included later in the finite element analysis, and the inclined rotor fault has been neglected. The machine with no defects will be called "initial design", whereas the machine with defects will be called "prototype".

Table 3. Main parameters of the 3D printer setup.

Printing speed	20 mm^3/s	Bed temperature	70 °C
Infill	30%	Nozzle temperature	200 °C

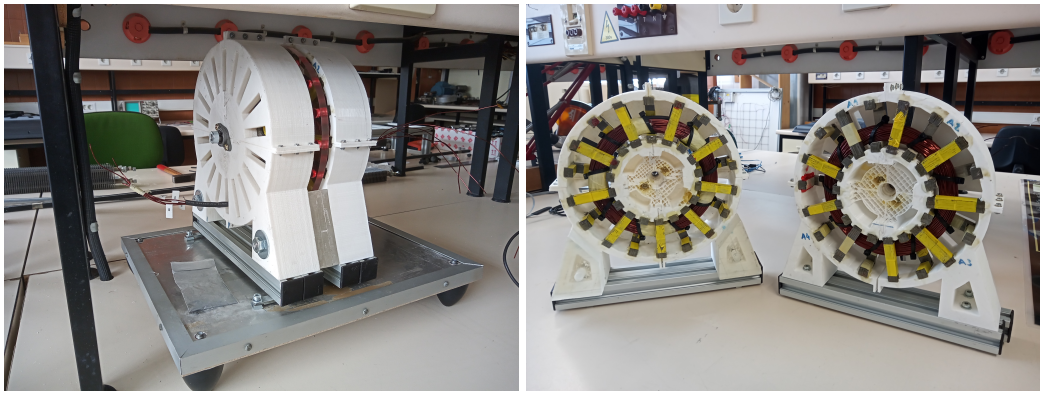

(**a**) (**b**)

(**c**) (**d**)

Figure 7. Detailed views of the TPAGTFG prototype: (**a**) overview, (**b**) the two stators with 90 electrical degrees shift, (**c**) one of the stators and the rotor during the assembly, and (**d**) stator and rotor with the iron cores, before and after removing the central iron column and the welds.

Furthermore, the B-H curve of the iron sheets has also been measured in a test sample: the material properties are unknown because the iron sheets come from reused transformers.

Figure 8a shows the experimental setup, based on a R-C series circuit. The H field in the secondary winding (H_3) can be calculated with (5), i.e., the solution of the magnetic circuit in Figure 8b for branch number 3. The corresponding B field (B_3) is given by the R-C series circuit connected to the secondary side (6). N_1 and N_2 are the number of turns of the primary and secondary winding, respectively; R_1 and R_2 are the series resistances of the primary and secondary; U_{R1} is the voltage drop across R_1; L_3 and S_3 are the length and the cross-section of branch number 3 in the magnetic circuit; C is the series capacitance at the secondary winding; and U_C is the voltage drop across C. Finally, the experimental B-H curve is shown in Figure 8c, where the relative permeability has also been depicted.

$$H_3 = \frac{18N_1U_{R1}}{117R_1L_3} \tag{5}$$

$$B_3 = \frac{R_2CU_c}{N_2S_3} \tag{6}$$

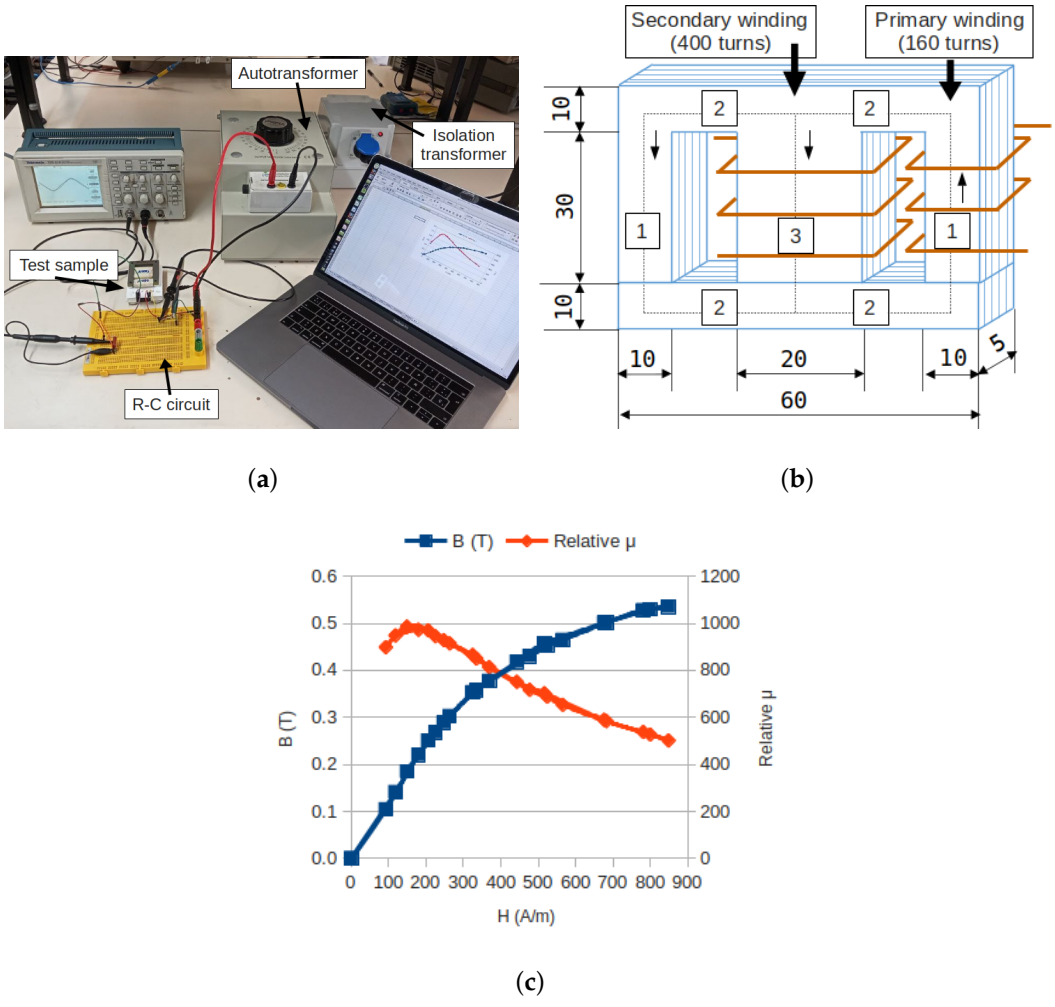

Figure 8. B-H curve measurement: (**a**) experimental setup, (**b**) magnetic circuit, and (**c**) B-H curve.

Copper windings are characterized by its resistance and inductance. The toroidal coil of conventional TFMs can be defined by the mean fiber diameter (D_c), the cross-section area (S_{cs}), and the fill factor (k_f), so the resistance (R) is given by (7). For a given characteristic length of the cross-section (D_{cs}), and if the wire diameter is D_w, the fill factor depends on whether the cross-section is circular (8) or square shaped (9). Table 4 shows the experimental results of the resistance measurement: the square-shaped cross-section adapts better than the circular one to our handmade winding, and in fact the fill factor is quite close to the

optimal for 144 turns [38]. The synchronous inductance of the proposed TPAGTFG cannot be calculated analytically with great precision, because the leakage and fringing effects might be significant in the air gap, so it has been measured with an impedance meter.

$$R = N^2 \frac{\rho \pi D_c}{k_f S_{cs}} \tag{7}$$

$$k_{fc} = N \left(\frac{D_w}{D_{cs}} \right)^2 \tag{8}$$

$$k_{fs} = \frac{\pi}{4} k_{fc} \tag{9}$$

Table 4. Coil parameters.

Mean fiber diameter	145 mm	Resistance (calculated)	0.667 Ω
Characteristic length	17 mm	Resistance (measured)	0.662 Ω
Fill factor (square section)	0.823	Synchronous inductance (measured)	7.76 mH
Optimal fill factor for 144 turns	0.837	Synchronous reactance at 500 rpm	3.65 Ω

3. Validation of the TPAGTFG Steady-State Operation

The TPAGTFG prototype has been validated during steady-state operation, using analytical equations, the magnetic equivalent circuit (MEC), and the finite element method (FEM). The phases misalignment and the rotor run-out fault have been included in the FEM model to analyze their influence. Moreover, experimental tests have been conducted throughout the investigation, both with no load and with several resistive loads. The MEC has been solved with MATLAB-Simulink, and the FEM software is Flux3D, from Altair.

3.1. Analytical Equations

If the flux density distribution in the air gap is assumed to be rectangular, the peak value ($B_{g1,pk}$) and the mean value ($B_{g1,avg}$) of the first harmonic can be estimated by (10) and (11). B_r is the remanent flux density of the PMs, W_{PM} is the axial length of the PMs, G is the air gap length, and k_m is the fraction of the poles covered by the PMs. k_m is different for the upper and lower PMs, as the circumferential pole pitch increases with the radius, so the mean value for the upper and lower PMs has been used. Therefore, the PMs flux linkage (Ψ_{PM}) and the back-electromotive force (back-EMF, E_0) can be calculated with (12) and (13), where N is the number of turns, p is the number of pole pairs, S_{PM} is the PMs cross-section, S_U is the U-core cross section, and n is the mechanical speed in rpm. The analytical results are shown in Table 5.

$$B_{g1,pk} = \frac{4}{\pi} B_r \frac{W_{PM}}{W_{PM} + 2G} \sin\left(k_m \frac{\pi}{2}\right) \tag{10}$$

$$B_{g1,avg} = \frac{2}{\pi} B_{g1,pk} \tag{11}$$

$$\Psi_{PM} = N p B_{g1,avg} \frac{S_{PM} + S_U}{2} \tag{12}$$

$$E_0 = \frac{1}{\sqrt{2}} n \frac{2\pi}{60} p \Psi_{PM} \tag{13}$$

Table 5. Results of the analytical calculations.

Average flux density in the air gap ($B_{g1,avg}$)	0.093 T
PMs flux linkage, peak value (Ψ_{PM})	0.0113 Wb
Back-EMF, RMS value (E_0)	3.77 V

3.2. Magnetic Equivalent Circuit

Magnetic equivalent circuits (MECs) are generally used in electric machines design and optimization due to their low computational cost, but their precision is lower than that of the FEM. When dealing with axial flux machines and transverse flux machines, the magnetic flux path is divided into volumes (prisms, cylinders, spheres, rings, and fractions of them) and the conductances (G) are calculated using classical formulae [39]. In this work, the following conductances have been used: prism with cross section wL and axial length g (14), half-cylinder of axial length L (15), quarter-sphere with diameter g (16) and half-ring with axial length L, inner diameter g, and width w with $g < 3w$ (17). μ is the magnetic permeability.

$$G = \mu \frac{wL}{g} \tag{14}$$

$$G = 0.26 \mu L \tag{15}$$

$$G = 0.077 \mu g \tag{16}$$

$$G = \mu \frac{L}{\pi} \ln\left(1 + \frac{2w}{g}\right) \tag{17}$$

Figure 9 illustrates the leakage, fringing and "back-coupling" conductance paths that have been adopted in the proposed MEC of the TPAGTFM, based on preliminary FEM simulations. Notice that the cylindrical PMs have been firstly transformed (18) in an equivalent square prism (side L_{PM}) with the same cross-section that the original cylinder (diameter D_{PM}). The back-coupling path corresponds to the rear faces of the PMs that are not facing the iron core in the maximum linkage position: in these faces the magnetic flux closes through the air. Furthermore, each of the flux paths is associated with a volume, as shown in the left corner of Figure 9, where the half-cylinder and the quarter-sphere have been depicted. Proceeding in a similar way with the rest of the flux paths, the MEC depicted in Figure 10 is proposed. The flux paths of the TPAGTFM are decomposed as shown in Table 6, and the reluctances of the MEC are calculated with (19)–(26): back-coupling paths (R_{BC}), permanent magnets (R_{PM}), self-leakage of the PMs ($R_{PM,LS}$), mutual-leakage of the PMs ($R_{PM,LM}$), U- and I-cores (R_U, R_I), gap (R_G), and gap fringing ($R_{G,F}$). The magnetomotive force (HL) of the PMs is calculated with (27). Therefore, the flux Φ through the air gap (the ammeter in Figure 10) and the flux linkage Ψ_{PM} can be obtained (28). The MEC solution of the initial design is presented in Table 7. It is shown that the flux linkage and the back-EMF obtained through the MEC are slightly lower than the analytical calculation (Table 5). Here the leakage, fringing, and back-coupling paths have been included in the model, and they have a non-negligible effect in the proposed TPAGTFM, where the equivalent air gap is large and the magnetic flux closes through the air.

$$L_{PM} = \frac{D_{PM}}{2} \sqrt{\pi} \tag{18}$$

$$R_{BC} = \frac{1}{G_{BC,1} + G_{BC,2}} \tag{19}$$

$$R_{PM} = \frac{1}{G_{PM}} \tag{20}$$

$$R_{PM,LS} = \frac{1}{4G_{PM,LS,1} + 4G_{PM,LS,2}} \tag{21}$$

$$R_{PM,LM} = \frac{1}{G_{PM,LM}} \tag{22}$$

$$R_U = \frac{1}{G_U} \tag{23}$$

$$R_I = \frac{1}{G_I} \tag{24}$$

$$R_G = \frac{1}{G_G} \tag{25}$$

$$R_{G,F} = \frac{1}{4G_{G,F1} + 4G_{G,F2}} \tag{26}$$

$$HL = \frac{B_r}{\mu} W_{PM} \tag{27}$$

$$\Psi_{PM} = Np\Phi \tag{28}$$

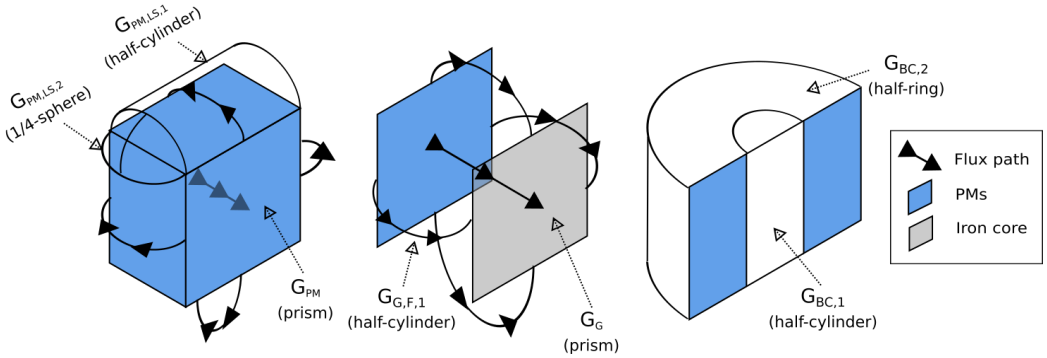

Figure 9. Leakage (**left**), fringing (**center**), and back-coupling (**right**) paths for the PMs and the air gap.

Table 6. Decomposition of the flux path in volumes to calculate the conductances.

Group	Nomenclature	Conductance
Back-coupling paths	$G_{BC,1}$	Half-cylinder
	$G_{BC,2}$	Half-ring
Permanent magnets	G_{PM}	Prism
	$G_{PM,LS,1}$	Half-cylinder
	$G_{PM,LS,2}$	Quarter-sphere
	$G_{PM,LM}$	Half-cylinder
Iron cores	G_U	Prism
	G_I	Prism
Air gap	G_G	Prism
	$G_{GF,1}$	Half-cylinder
	$G_{GF,2}$	Quarter-sphere

Table 7. Solution of the MEC for the initial design.

Average flux density in the air gap ($B_{g1,avg}$)	0.085 T
PMs flux linkage, peak value (Ψ_{PM})	0.0105 Wb
Back-EMF, RMS value (E_0)	3.48 V

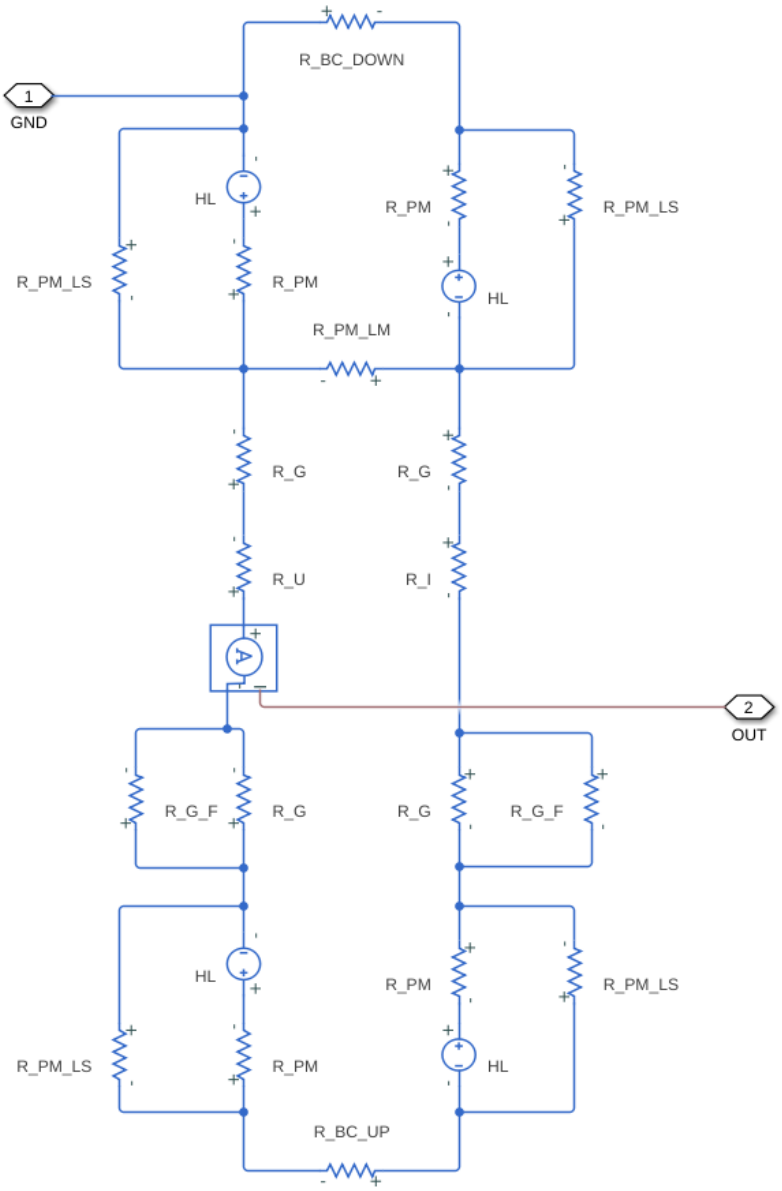

Figure 10. Magnetic equivalent circuit of the proposed TPAGTFG.

3.3. Description of the Finite Element Model

Figure 11 shows the meshed model of both the initial design and the prototype. The boundary conditions are: zero magnetic field at infinity (it is set by the FEM software through an "infinite box" transformation) and, for the initial design model, periodicity along the pole pairs (see Figure 11a). The prototype model (Figure 11b) has an angular shift of 130 electrical degrees between phases instead of 90 electrical degrees, so there is no angular periodicity and the whole machine must be modeled. As the magnetic flux paths are inherently three dimensional in TFMs, extruded mesh and second-order elements are a good combination in order to save computation time while obtaining accurate results.

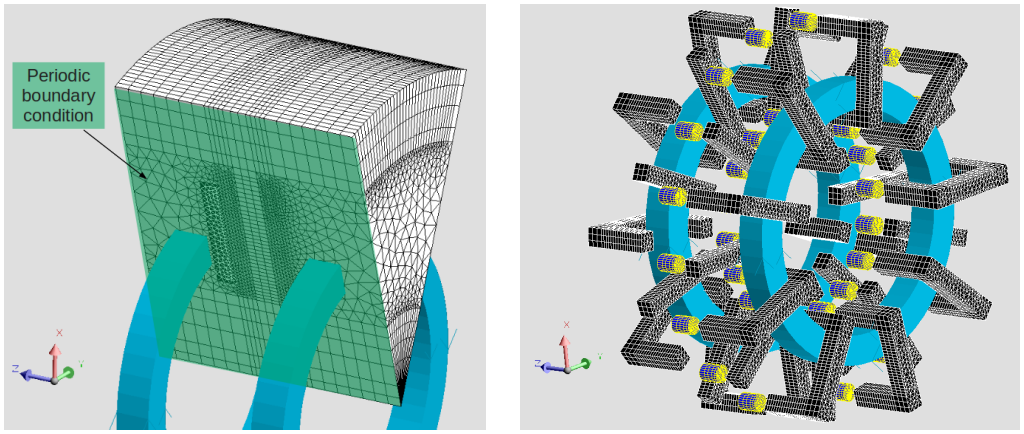

(**a**) (**b**)

Figure 11. Meshed models: (**a**) initial design with the infinite box removed and (**b**) prototype with the air volumes removed.

Furthermore, a mesh convergence analysis has been conducted over the initial design geometry to verify that the elements size does not affect the flux linkage value. The element size in a mesh line can be defined as a function of the number of elements in each coordinate, and subsequently the effects on the results can be analyzed through a parametric study. Figure 12 shows two cases in which the number of mesh elements along x, y, and z coordinates has changed. As the mesh has second-order elements, there are no appreciable deviations in the flux linkage values that are obtained, so the coarsest mesh can be used in the following simulations, thus saving computation time.

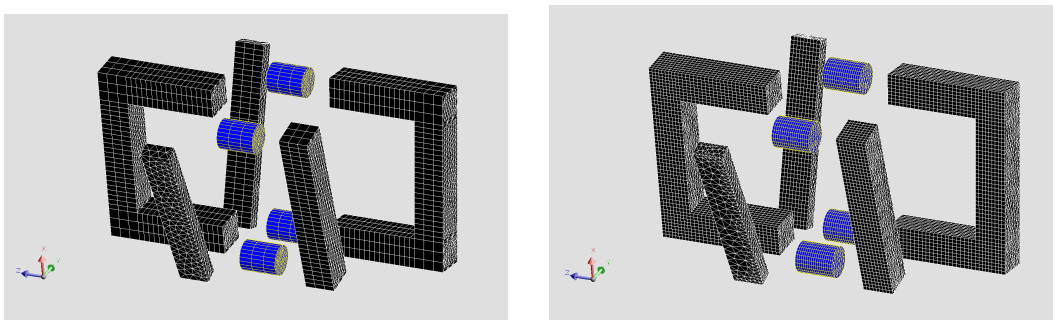

(**a**) (**b**)

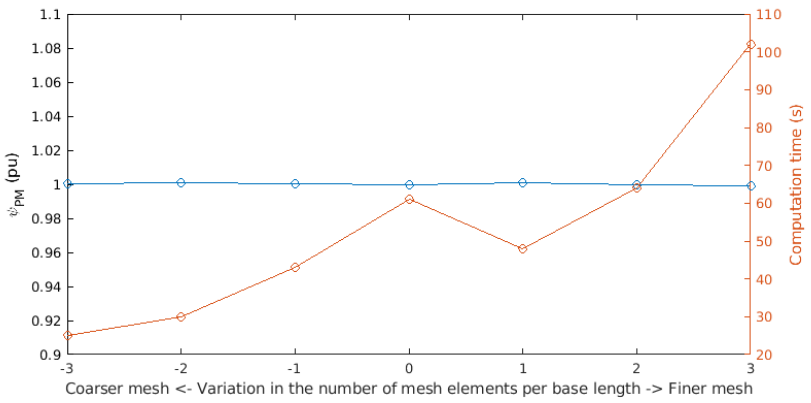

(**c**)

Figure 12. Mesh convergence analysis: (**a**) illustration of the coarsest mesh, (**b**) illustration of the finest mesh, and (**c**) impact of the number of elements on the flux linkage.

3.4. Magnetostatic Finite Element Model and Experiments

A magnetostatic FEM simulation has been run both for the "initial design" (with no defects) and the "prototype" (with misalignment and run-out fault) in order to compare the flux linkage and back-EMF values with the analytical calculations and the MEC. A parametric study has been conducted to evaluate the effect of the PM flux density, given by the PM material and the quality assurance in the manufacturing process, on the flux linkage and the back-EMF. Figure 13 shows the results, both for the initial design and for the prototype. As the air gap of the proposed TFM is large, the iron is not saturated and the PMs flux linkage turns out to be linear with the remanent flux density: the same results have been obtained with FEM with linear and nonlinear iron.

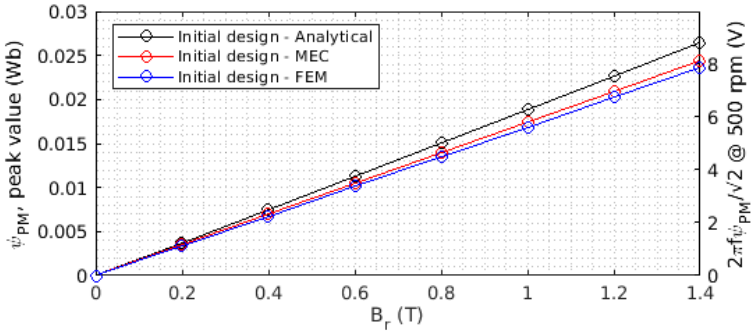

(**a**)

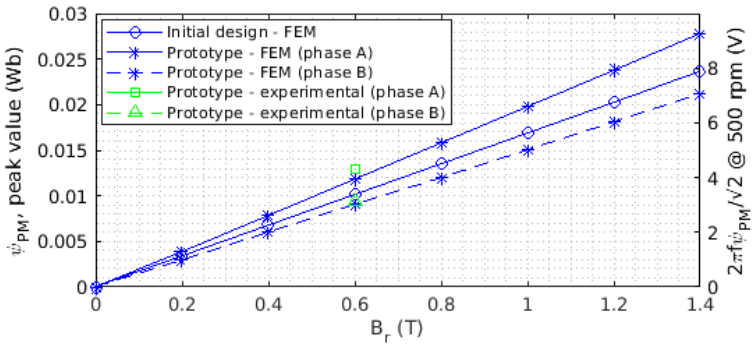

(**b**)

Figure 13. Magnetostatic FEM results with respect to the remanent flux density and comparison: (**a**) initial design and (**b**) prototype.

According to Figure 13a, in the initial design and with no defects, the MEC and the FEM show a very good agreement, and the analytical values are near 12% higher than the FEM results. Therefore, in the proposed TPAGTFG prototype the flux linkage is mainly determined by the remanent flux density of the PMs, the PMs volume, and the air gap length, but the leakage, fringing, and back-coupling paths seem to have a significant impact on the magnetic field distribution. In any case, their effects have been well captured by the proposed MEC. The FEM simulation also shows that the flux density in the air gap (B_g) is not sinusoidal (see Figure 14), as the previous first-harmonic analytical calculation assumes, and in fact the flux density waveform is not the same in the lower and upper PMs: the pole pitch length is 1.8 times higher in the upper PMs, and it affects the magnetic field distribution via leakage and fringing. Moreover, the peak value of the flux density is 12% higher in the analytical waveform; it is the same deviation as in the flux linkage.

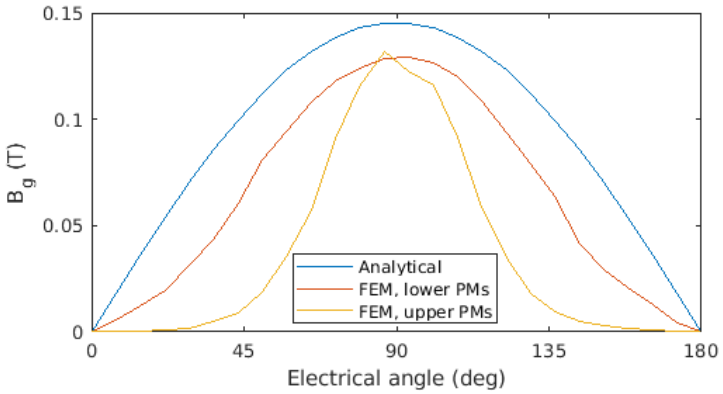

Figure 14. Flux density distribution in the air gap.

In Figure 13b the results of the FEM model of the "prototype" have been depicted, together with the experimental results—in the latter case the flux linkage has been calculated from the no load test with (13). The misalignment and the run-out fault lead to a deviation from the "initial design" FEM model about 17% in phase A and −10% in phase B. Moreover, the FEM model of the "prototype" shows good agreement with the experimental results: −8.5% error in phase A and −3.7% in phase B. The differences between phase A and phase B in the FEM model with respect to the real prototype could be attributed to some uncertainty when measuring the air gap in the assembled prototype with the caliper, considering that the air gap length is both affected by the run-out fault and the inclined rotor fault. Figure 15 shows a FEM analysis with respect to the air gap length: 9 and 11 mm were adopted in the prototype characterization, but according the to the FEM model, the real air gaps of the prototype might be around 8.4 and 10.7 mm.

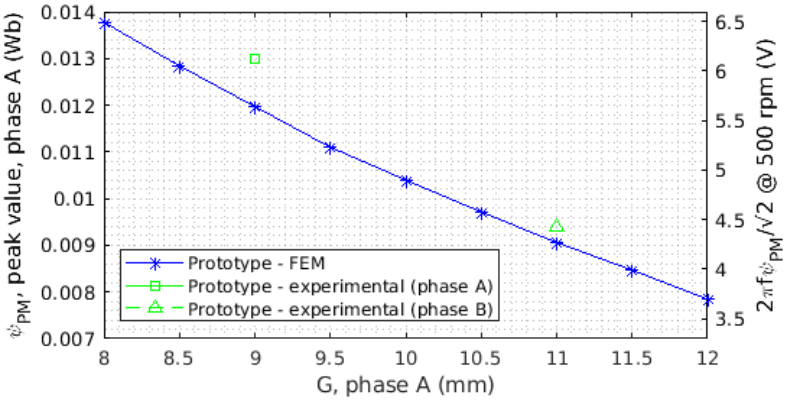

Figure 15. Magnetostatic FEM results with respect to the air gap length.

3.5. Transient Finite Element Model and Experiments

Figure 16 shows the test bench for the TPAGTFM experimental validation. No load and load tests have been conducted, the former to analyze the flux linkage and the back-EMF, and the latter to obtain the output voltage with different resistive loads (unity power factor test). In Figure 17, the back-EMF waveforms from the FEM model and the experimental tests have been depicted. It is shown that the back-EMF is sinusoidal and the peak value is slightly higher in the FEM model, as previously discussed. Moreover, it is shown that the there is a shift between phase A and phase B around 130 electrical degrees, thus confirming the angular misalignment that was detected during the prototype characterization. The misalignment between phases could be reduced with more precise machining tools or with a more resistant material against machining. Tables 8 and 9 show the comparison of the flux linkage and back-EMF results from different methods. The error with respect to the prototype measurements is lower than 10% in all cases except the MEC in phase

A and the analytical calculation in phase B, where the error is near 20% and the machine defects were not considered. Finally, Figure 18 shows the output voltage and current in the unity power factor test (resistive load). The current density is lower than 0.5 A/mm^2, so the temperature raise due to copper losses does not affect the PLA stability. There is a significant difference between phase A and phase B outputs due to the eccentricity of the rotor, and it should be carefully controlled in future models of the prototype with the use of more precise manufacturing equipment. The synchronous inductance (L) can be calculated from the no load and load tests using the equivalent circuit of a synchronous machine (29), and the obtained value is 8.5 mH, similar to the characterization value shown in Table 4. As the rotor has no iron or SMC poles, the stator inductance is not affected by the rotor position.

$$L = \frac{1}{\omega}\sqrt{\left(\frac{E_0}{I}\right)^2 - (R + R_{load})^2} \tag{29}$$

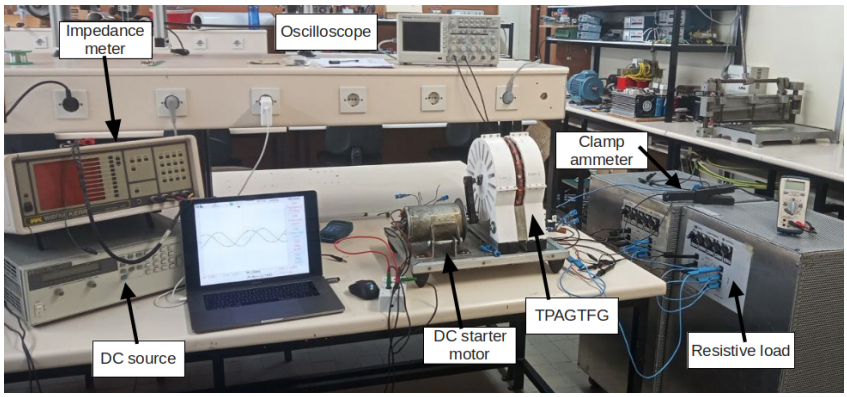

Figure 16. Test bench for the TPAGTFM experimental validation.

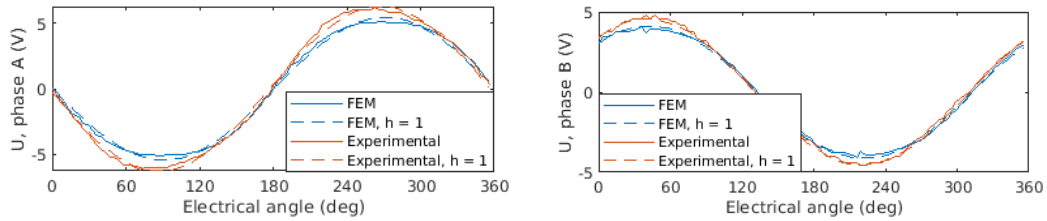

(**a**) (**b**)

Figure 17. Back-EMF waveforms of the FEM simulation and the experimental results of the prototype: (**a**) phase A and (**b**) phase B.

Table 8. Flux linkage and back-EMF at 500 rpm: comparison for phase A.

	Analytical	MEC	Magnetostatic FEM	Transient FEM	Experimental
Ψ_{PM}	0.0113 Wb	0.0105 Wb	0.0119 Wb	0.0116 Wb	0.0130 Wb
E_0	3.77 V	3.50 V	3.99 V	3.86 V	4.33 V

Table 9. Flux linkage and back-EMF at 500 rpm: comparison for phase B.

	Analytical	MEC	Magnetostatic FEM	Transient FEM	Experimental
Ψ_{PM}	0.0113 Wb	0.0105 Wb	0.0091 Wb	0.0088 Wb	0.0094 Wb
E_0	3.77 V	3.50 V	3.13 V	2.92 V	3.13 V

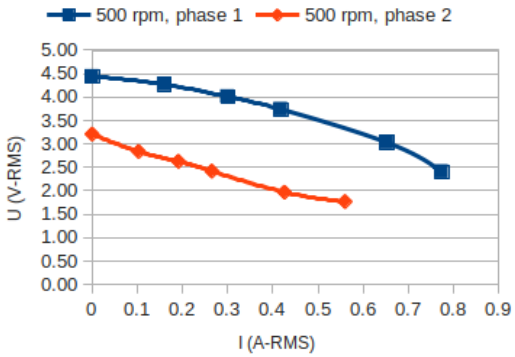

Figure 18. Output voltage and current in the unity power factor test.

4. Conclusions

The prototype of a two-phase axial-gap transverse flux generator with reused materials and 3D printing has been validated in this paper using analytical equations, the magnetic equivalent circuit, the finite element method (magnetostatic and transient), and experimental tests, with no load and with resistive loads. The prototype has a large air gap in order to reduce the cogging torque and vibrations for mechanical stability.

After the prototype design and characterization, analytical equations and the magnetic equivalent circuit have been proposed for the steady-state validation of the novel TPAGTFG with no manufacturing defects, and they show a good agreement with the FEM model. The static FEM simulations show that the flux linkage of the TPAGTFG mainly depends on the air gap flux density and the PMs volume, even though in this topology the flux path closes through the air. Moreover, the leakage, fringing, and back-coupling paths have a non-negligible influence on the flux density distribution in the air-gap and, therefore, in the back-EMF, but these effects have been modeled accurately by the proposed magnetic equivalent circuit.

The angular misalignment of the phases and the rotor eccentricity (run-out fault and inclined rotor faults) must be carefully considered during the manufacturing process of such kind of transverse flux machines, and it requires precise manufacturing tools. Once the manufacturing defects of the prototype are included in the finite element models, the computational results show good agreement with the experimental tests.

Author Contributions: Conceptualization, V.B.-B. and J.A.D.-N.; methodology, J.S.A.-S.; software, V.B.-B.; validation, V.B.-B., J.S.A.-S. and J.A.D.-N.; formal analysis, V.B.-B.; investigation, V.B.-B.; resources, J.S.A.-S. and J.A.D.-N.; writing—original draft preparation, V.B.-B.; writing—review and editing, J.S.A.-S. and J.A.D.-N.; visualization, V.B.-B.; supervision, J.S.A.-S. and J.A.D.-N. All authors have read and agreed to the published version of the manuscript.

Funding: This work was supported in part by the Spanish Ministry of Universities under Grant FPU20/03436.

Acknowledgments: The authors would like to acknowledge the invaluable help of José Carlos Millán de Cortés, lab technician of the Department of Electrical Engineering, University of Zaragoza, during the prototype assembly. Furthermore, thanks to José Ángel Pardo Gracia, from the Materials Science Area, University of Zaragoza, for providing the gaussmeter. Additionally, authors would like to acknowledge the use of Servicio General de Apoyo a la Investigación-SAI, Universidad de Zaragoza.

Conflicts of Interest: The authors declare no conflict of interest.

References

1. Kumar, R.; Zhu, Z.Q.; Duke, A.; Thomas, A.; Clark, R.; Azar, Z.; Wu, Z.Y. A Review on Transverse Flux Permanent Magnet Machines for Wind Power Applications. *IEEE Access* **2020**, *8*, 216543–216565. [CrossRef]
2. Ballestín-Bernad, V.; Artal-Sevil, J.S.; Domínguez-Navarro, J.A. A Review of Transverse Flux Machines Topologies and Design. *Energies* **2021**, *14*, 7173. [CrossRef]

3. Bensalah, A.; Barakat, G.; Amara, Y. Electrical Generators for Large Wind Turbine: Trends and Challenges. *Energies* **2022**, *15*, 6700. [CrossRef]
4. Keller, M.; Parspour, N. Experimental identification and validation of model parameters of a permanent magnetic excited transverse flux machine for robotic applications. In Proceedings of the 2017 11th IEEE International Conference on Compatibility, Power Electronics and Power Engineering, CPE-POWERENG 2017, Cadiz, Spain, 4–6 April 2017; pp. 352–357. [CrossRef]
5. Dobzhanskyi, O.; Gouws, R.; Amiri, E. Analysis of PM Transverse-Flux Outer Rotor Machines with Different Configuration. *IEEE Trans. Ind. Appl.* **2017**, *53*, 4260–4268. [CrossRef]
6. Dobzhanskyi, O.; Gouws, R.; Amiri, E. Comparison analysis of AC PM transverse-flux machines of different designs in terms of power density and cost. In Proceedings of the 58th Annual International Scientific Confererence on Power and Electrical Engineering of Riga Technical University, RTUCON 2017—Proceedings, Riga, Latvia, 12–13 October 2017; pp. 1–6. [CrossRef]
7. Dobzhanskyi, O.; Gouws, R.; Amiri, E. On the Role of Magnetic Shunts for Increasing Performance of Transverse Flux Machines. *IEEE Trans. Magn.* **2017**, *53*. [CrossRef]
8. Lv, C.; Zhang, L.; Xu, Y.; Liu, Y. Research on novel high torque density transverse-flux permanent magnet motor. In Proceedings of the 2019 22nd International Conference on Electrical Machines and Systems, ICEMS 2019, Harbin, China, 11–14 August 2019. [CrossRef]
9. Pourmoosa, A.A.; Mirsalim, M. A Transverse Flux Generator with a Single Row of Permanent Magnets: Analytical Design and Performance Evaluation. *IEEE Trans. Ind. Electron.* **2019**, *66*, 152–161. [CrossRef]
10. Peng, G.; Wei, J.; Shi, Y.; Shao, Z.; Jian, L. A Novel Transverse Flux Permanent Magnet Disk Wind Power Generator with H-Shaped Stator Cores. *Energies* **2018**, *11*, 810. [CrossRef]
11. Husain, T.; Hasan, I.; Sozer, Y.; Husain, I.; Muljadi, E. Cogging torque minimization in transverse flux machines. *IEEE Trans. Ind. Appl.* **2019**, *55*, 385–397. [CrossRef]
12. Nasiri-Zarandi, R.; Ajamloo, A.M.; Abbaszadeh, K. Design Optimization of a Transverse Flux Halbach-Array PM Generator for Direct Drive Wind Turbines. *IEEE Trans. Energy Convers.* **2020**, *35*, 1485–1493. [CrossRef]
13. Nasiri-Zarandi, R.; Toulabi, M.S.; Karami-Shahnani, A. Two-Segment Magnet Transverse Flux Ferrite PM Generator for Direct-Drive Wind Turbine Applications: Nonlinear 3-D MEC Modeling and Experimental Validation. *IEEE Trans. Energy Convers.* **2022**, *37*, 1834–1843. [CrossRef]
14. Hui, J.; Gao, M.; Wang, Y. Design and optimisation of transverse flux machine with passive rotor and flux-concentrating structure. *IET Electr. Power Appl.* **2019**, *13*, 922–931. [CrossRef]
15. Yang, X.; Kou, B.; Luo, J.; Zhang, H. Electromagnetic Design of a Dual-Consequent-Pole Transverse Flux Motor. *IEEE Trans. Energy Convers.* **2020**, *35*, 1547–1558. [CrossRef]
16. Rabenstein, L.; Schmidt, M.; Dietz, A.; Parspour, N. Design, Construction and Measurement of a Laminated Transverse Flux Machine. In Proceedings of the 2022 International Conference on Electrical Machines (ICEM), Valencia, Spain, 5–8 September 2022; pp. 1197–1203. [CrossRef]
17. Azarinfar, H.; Aghaebrahimi, M.R. Design, Analysis and Fabrication of a Novel Transverse Flux Permanent Magnet Machine with Disk Rotor. *Appl. Sci.* **2017**, *7*, 860. [CrossRef]
18. Wang, M.; Zheng, P.; Tong, C.; Zhao, Q.; Qiao, G. Research on a Transverse-Flux Brushless Double-Rotor Machine for Hybrid Electric Vehicles. *IEEE Trans. Ind. Electron.* **2019**, *66*, 1032–1043. [CrossRef]
19. Kulan, M.C.; Baker, N.J.; Turvey, S. Manufacturing Challenges of a Modular Transverse Flux Alternator for Aerospace. *Energies* **2020**, *13*, 4275. [CrossRef]
20. Kulan, M.C.; Baker, N.J.; Turvey, S. Impact of Manufacturing and Material Uncertainties in Performance of a Transverse Flux Machine for Aerospace. *Energies* **2022**, *15*, 7607. [CrossRef]
21. Jordan, S.; Baker, N.J. Comparison of two transverse flux machines for an aerospace application. In Proceedings of the 2017 IEEE International Electric Machines and Drives Conference, IEMDC 2017, Miami, FL, USA, 21–24 May 2017. [CrossRef]
22. Baker, N.J.; Jordan, S. Comparison of Two Transverse Flux Machines for an Aerospace Application. *IEEE Trans. Ind. Appl.* **2018**, *54*, 5783–5790. [CrossRef]
23. Pourmoosa, A.A.; Ghods, M.; Faiz, J.; Vaez-Zadeh, S. Diagnosis and detection of dynamic eccentricity fault for permanent magnet transverse flux generator. *IET Electr. Power Appl.* **2021**, *15*, 528–541. [CrossRef]
24. Hasan, I.; Husain, T.; Sozer, Y.; Husain, I.; Muljadi, E. Mechanical performance of transverse flux machines. *IEEE Trans. Ind. Appl.* **2019**, *55*, 3716–3724. [CrossRef]
25. Hasan, I.; Chowdhury, A.; Sozer, Y. Effect of Pole Shaping on Cogging Torque, Torque Ripple and Vibrational Performance in Consequent Pole TFM. In Proceedings of the 2018 IEEE Energy Conversion Congress and Exposition, ECCE 2018, Portland, OR, USA, 23–27 September 2018; pp. 7330–7335. [CrossRef]
26. Vaimann, T.; Kallaste, A. Additive Manufacturing of Electrical Machines-Towards the Industrial Use of a Novel Technology. *Energies* **2023**, *16*, 544. [CrossRef]
27. Wrobel, R.; Mecrow, B. Additive manufacturing in construction of electrical machines-a review. In Proceedings of the 2019 IEEE Workshop on Electrical Machines Design, Control and Diagnosis, WEMDCD 2019, Athens, Greece, 22–23 April 2019; pp. 15–22. [CrossRef]
28. Wrobel, R.; Mecrow, B. A Comprehensive Review of Additive Manufacturing in Construction of Electrical Machines. *IEEE Trans. Energy Convers.* **2020**, *35*, 1054–1064. [CrossRef]

29. Naseer, M.U.; Kallaste, A.; Asad, B.; Vaimann, T.; Rassõlkin, A. A Review on Additive Manufacturing Possibilities for Electrical Machines. *Energies* **2021**, *14*, 1940. [CrossRef]
30. Hieke, S.; Stamann, M.; Lagunov, D.; Leidhold, R.; Masliennikov, A.; Duniev, A.; Yehorov, A. Two-phase transverse flux machine with disc rotor for high torque low speed Application. In Proceedings of the 2017 19th European Conference on Power Electronics and Applications, EPE 2017 ECCE Europe, Warsaw, Poland, 11–14 September 2017. [CrossRef]
31. Akinora, T. TFM 8—3d Printed Transverse Flux Generator by TanyaAkinora—Thingiverse. 2018. Available online: https://www.thingiverse.com/thing:2759924/makes (accessed on 17 November 2022).
32. Masliennikov, A.; Yehorov, A.; Duniev, O.; Leidhold, R.; Stamann, M.; Hieke, S. The magnetic system analysis of the transverse flux machine and its improvement. In Proceedings of the 2019 IEEE 2nd Ukraine Conference on Electrical and Computer Engineering, UKRCON 2019, Lviv, Ukraine, 2–6 July 2019; pp. 552–555. [CrossRef]
33. Commission, E. A New Circular Economy Action Plan. 2020. Available online: https://eur-lex.europa.eu/legal-content/EN/TXT/?uri=COM:2020:98:FIN (accessed on 22 November 2022).
34. Alatalo, M.; Lundmark, S.T.; Grunditz, E.A. Electric machine design for traction applications considering recycling aspects-review and new solution. In Proceedings of the IECON Proceedings (Industrial Electronics Conference), Melbourne, VIC, Australia, 7–10 November 2011; pp. 1836–1841. [CrossRef]
35. Artal-Sevil, J.S.; Dufo, R.; Dominguez, J.A.; Bernal-Agustin, J.L. Small wind turbines in smart grids. Transformation of electrical machines in permanent magnet synchronous generators. In Proceedings of the 2018 13th International Conference on Ecological Vehicles and Renewable Energies, EVER 2018, Monte Carlo, Monaco, 10–12 April 2018; pp. 1–8. [CrossRef]
36. Ballestín-Bernad, V.; Artal-Sevil, J.S.; Domínguez-Navarro, J.A. Analytical Optimal Design of a Two-Phase Axial-Gap Transverse Flux Motor. *Energies* **2021**, *14*, 3666. [CrossRef]
37. Boldea, I. *Variable Speed Generators*, 1st ed.; CRC Press: Boca Raton, FL, USA, 2006; p. 550.
38. Specht, E. The Best Known Packings of Equal Circles in a Square (Up to N = 10,000). Available online: http://www.packomania.com/ (accessed on 12 December 2022).
39. Gieras, J.F.; Wang, R.J.; Kamper, M.J. *Axial Flux Permanent Magnet Brushless Machines*, 2nd ed.; Springer Science & Business Media: Berlin/Heidelberg, Germany, 2008; pp. 1–362. [CrossRef]